

Gamma-ray diagnostics of Type Ia supernovae

Predictions of observables from three-dimensional modeling

A. Summa¹, A. Ulyanov², M. Kromer³, S. Boyer¹, F. K. Röpkke¹, S. A. Sim⁴, I. R. Seitenzahl^{1,3}, M. Fink¹,
K. Mannheim¹, R. Pakmor⁵, F. Ciaraldi-Schoolmann³, R. Diehl⁶, K. Maeda⁷, and W. Hillebrandt³

¹ Institut für Theoretische Physik und Astrophysik, Universität Würzburg, Campus Hubland Nord, Emil-Fischer-Str. 31,
D-97074 Würzburg, Germany

e-mail: asumma@astro.uni-wuerzburg.de

² School of Physics, University College Dublin, Belfield, Dublin 4, Ireland

³ Max-Planck-Institut für Astrophysik, Karl-Schwarzschild-Str. 1, D-85741 Garching, Germany

⁴ Research School of Astronomy and Astrophysics, The Australian National University, Mount Stromlo Observatory, Cotter Road,
Weston Creek, ACT 2611, Australia

⁵ Heidelberger Institut für Theoretische Studien, Schloss-Wolfsbrunnenweg 35, D-69118 Heidelberg, Germany

⁶ Max-Planck-Institut für extraterrestrische Physik, Giessenbachstraße, D-85748 Garching, Germany

⁷ Kavli Institute for the Physics and Mathematics of the Universe (Kavli-IPMU), Todai Institutes for Advanced Study (TODIAS),
University of Tokyo, 5-1-5 Kashiwanoha, Kashiwa, Chiba 277-8583, Japan

Received xxxx xx, xxxx / accepted xxxx xx, xxxx

ABSTRACT

Context. Although the question of progenitor systems and detailed explosion mechanisms still remains a matter of discussion, it is commonly believed that Type Ia supernovae (SNe Ia) are production sites of large amounts of radioactive nuclei. Besides the fact that the gamma-ray emission due to radioactive decays is responsible for powering the light curves of SNe Ia, gamma rays themselves are of particular interest as a diagnostic tool because they provide a direct way to obtain deeper insights into the nucleosynthesis and the kinematics of these explosion events.

Aims. We study the evolution of gamma-ray line and continuum emission of SNe Ia with the objective to analyze the relevance of observations in this energy range. We seek to investigate the chances for success of future MeV missions regarding their capabilities of constraining intrinsic properties and physical processes of SNe Ia.

Methods. Focusing on two of the most broadly discussed SN Ia progenitor scenarios – a delayed detonation in a Chandrasekhar-mass white dwarf (WD) and a violent merger of two WDs – we use three-dimensional explosion models and perform radiative transfer simulations to obtain synthetic gamma-ray spectra. Both chosen models produce the same mass of ⁵⁶Ni and have similar optical properties that are in reasonable agreement with the recently observed supernova SN 2011fe. We examine the gamma-ray spectra with respect to their distinct features and draw connections to certain characteristics of the explosion models. Applying diagnostics, such as line and hardness ratios, the detection prospects for future gamma-ray missions with higher sensitivities in the MeV energy range are discussed.

Results. In contrast to the optical regime, the gamma-ray emission of our two chosen models proves to be rather different. The almost direct connection of the emission of gamma rays to fundamental physical processes occurring in SNe Ia permits additional constraints concerning several explosion model properties that are not easily accessible within other wavelength ranges. Proposed future MeV missions such as GRIPS will resolve all spectral details only for nearby SNe Ia, but hardness ratio and light curve measurements still allow for a distinction of the two different models at 10 and 16 Mpc for an exposure time of 10⁶ s, respectively. The possibility to detect the strongest line features up to the Virgo distance will offer the opportunity to build up a first sample of SN Ia detections in the gamma-ray energy range and underlines the importance of future space observatories for MeV gamma rays.

Key words. supernovae: general – hydrodynamics – nuclear reactions, nucleosynthesis, abundances – radiative transfer – gamma rays: general – line: formation

1. Introduction

While there is general agreement that SNe Ia are the result of thermonuclear explosions of carbon-oxygen WDs, many questions concerning the progenitor and explosion scenarios still remain open (cf. Hillebrandt & Niemeyer 2000). This lack of knowledge is contrasted by the relevance of SNe Ia for measuring cosmological distances as well as their influence on the chemical evolution of the universe and emphasizes the need of a more thorough understanding of the underlying physics. To constrain current explosion models as tightly as possible, a multi-

wavelength approach extending to the gamma-ray regime (MeV energies) is desirable.

The gamma-ray spectra of SNe Ia are dominated by the lines of the ⁵⁶Ni → ⁵⁶Co → ⁵⁶Fe decay chain which powers the observable display of SNe Ia. In contrast to studies in the optical or infrared wavelength regime where the emissivity is strongly dependent on the complex opacity structure which in turn depends on the atomic level populations and chemical composition, the emissivities in the gamma-ray regime are determined from their branching ratios and radioactive half-lives and a few rather simple interaction processes like pair-production,

Compton scattering and photo-electrical absorption. This makes the gamma-ray regime an ideal tool to obtain a more direct handle on the mass-velocity distribution of the explosion product (Milne et al. 2004). These very promising prospects have led to numerous theoretical efforts (mostly one-dimensional) in investigating the gamma-ray emission of SNe Ia in the past (see for instance Clayton et al. 1969; Clayton 1974; Ambwani & Sutherland 1988; Chan & Lingenfelter 1988, 1990, 1991; Burrows & The 1990; Müller et al. 1991; Höflich et al. 1992; Kumagai & Nomoto 1997; Gómez-Gomar et al. 1998; Höflich et al. 1998; Sim & Mazzali 2008; Isern et al. 2008; Kromer et al. 2010; Maeda et al. 2012). Although there have been first attempts of taking three-dimensional effects into account (e.g. Höflich 2002), a fully three-dimensional treatment of the explosion hydrodynamics as well as the radiation transfer calculations has not been carried out in previous SN Ia gamma-ray emission studies. We determine, to our knowledge for the first time, the predicted gamma-ray emission for completely three-dimensional SN Ia explosion models. The three-dimensional approach is important for a realistic description of the distribution of the radioactive isotopes and the surrounding ejecta material – both factors the gamma-ray emission of SNe Ia is sensitive for as shown in the following. Furthermore, a thorough investigation of line-of-sight effects due to different viewing angles relies on a three-dimensional treatment of the explosion scenario.

However, as of now the detection of SNe Ia at MeV energies has not been practicable owing to the low sensitivities or non-existence of detection instruments in this energy range. In this paper, we explore the additional benefits from the analysis of gamma-ray spectra towards a more sound theoretical understanding of SNe Ia and discuss the detection limits of proposed next generation gamma-ray observatories. For this aim to be achieved, we run full detector simulations of the proposed MeV satellite GRIPS (Greiner et al. 2012).

In this paper, we focus on two main branches of suggested SN Ia progenitor models: The explosion of a carbon-oxygen Chandrasekhar-mass WD and the super-Chandrasekhar-mass violent merger of two carbon-oxygen WDs. While the first scenario marks the end of a WD close to the Chandrasekhar limit that accretes mass from a companion star through Roche-lobe overflow or strong stellar winds, the second is considered to be the result of two closely orbiting WDs losing energy due to the emission of gravitational waves and merging finally. The latter scenario has attracted a renewed interest in the last years since, in contrast to previous thoughts, the publications by Pakmor et al. (2010, 2011, 2012a) demonstrated that *violent* mergers of two carbon-oxygen WDs can directly lead to a thermonuclear explosion while the merger is still ongoing. As an extension to preceding gamma-ray studies of SNe Ia, we discuss the gamma-ray emission of a violent merger for the first time.

Both scenarios generate optical observables that are similar to those of normal SNe Ia (Mazzali et al. 2007; Kasen et al. 2009; Blondin et al. 2011; Pakmor et al. 2012b; Röpke et al. 2012), in spite of significant differences in the total mass and the ejecta structure. Further observable distinctions through SNe Ia gamma-ray spectra would therefore provide an additional handle on the progenitor channel question.

The outline of the paper is as follows: In Sect. 2 we describe the applied explosion models and the radiative transfer scheme. After a discussion of the resulting gamma-ray spectra and a study of the applicability of different diagnostic tools in Sect. 3, we investigate the chances of detecting gamma-ray line emission from SNe Ia in the near future in Sect. 4 and conclude with a short summary of the main findings.

2. Simulation framework

2.1. Explosion models

In the first simulation, we calculate the gamma-ray emission for the explosion of a near Chandrasekhar-mass (M_{Ch}) WD as a delayed detonation (e.g. Khokhlov 1991). After an initial subsonic deflagration phase of nuclear burning that produces mainly iron group elements, the explosion turns into a supersonic detonation. The remaining fuel is mostly burned to intermediate mass elements due to the prevailing lower densities caused by the energy release of the deflagration mode and the subsequent expansion of the star. We use the N100 model from the set of three-dimensional delayed detonation simulations carried out by Seitzzahl et al. (2013) with the thermonuclear supernova code LEAFS. For a detailed description of the applied techniques we refer the reader to Reinecke et al. (1999), Röpke & Hillebrandt (2005), Schmidt et al. (2006), Röpke & Niemeyer (2007) and references therein. We chose the N100 model since it produces optical observables that closely resemble those of “normal” SNe Ia (Röpke et al. 2012). The model is based on an isothermal non-rotating WD in hydrostatic equilibrium with a central density of $\rho_c = 2.9 \times 10^9 \text{ g cm}^{-3}$. During the explosion, 10^6 tracer particles reproducing the underlying density profile of the WD record the thermodynamic conditions. We then use the information provided by the tracer particles to calculate the detailed isotopic composition in a post-processing step with a reaction network of 384 nuclides (Travaglio et al. 2004; Röpke et al. 2006; Seitzzahl et al. 2010). The initial chemical composition is assumed to be 47.5 % ^{12}C , 50.0 % ^{16}O and 2.5 % ^{22}Ne by mass, resulting in an electron fraction of $Y_e = 0.498864$, which corresponds to a zero-age main sequence metallicity comparable to that of the Sun. With a kinetic energy of $1.45 \times 10^{51} \text{ erg}$ and a total mass of $1.40 M_{\odot}$ of the ejecta, N100 produced $0.604 M_{\odot}$ of ^{56}Ni . Roughly half of the ^{56}Ni is located in the inner $0.3 M_{\odot}$ at velocities below $4,000 \text{ km s}^{-1}$, while the other half is more or less isotropically but inhomogeneously distributed within the remainder of the inner $\sim 1.2 M_{\odot}$, out to velocities of $12,000 \text{ km s}^{-1}$.

The second simulation is the violent merger of a $1.1 M_{\odot}$ and a $0.9 M_{\odot}$ WD of Pakmor et al. (2012b). Again, this model reproduces the features of “normal” SNe Ia at optical wavelengths (Röpke et al. 2012). To model the inspiral and the merger, Pakmor et al. (2012a) used a modified version of the SPH code GADGET (Springel 2005). Both WDs are constructed from a total of 1.8×10^6 particles of equal mass. After a relaxation phase, the distance between the WDs is slowly decreased according to the method of Dan et al. (2011) until the first particle of the less massive (secondary) WD reaches the Lagrangian point between the two objects. This triggers the actual simulation to start. During its progress, more and more material from the secondary WD is accreted and heated up on the surface of the primary, giving rise to the formation of hot spots and the ignition of carbon burning. Following the guidelines of microscopic detonation simulations (Seitzzahl et al. 2009), a detonation is initiated in a hot spot that reaches a temperature of more than $2.5 \times 10^9 \text{ K}$ and a density of about $2 \times 10^6 \text{ g cm}^{-3}$. The mapping of the actual simulation to a uniform Cartesian grid with $768 \times 768 \times 768$ cells and a total box size of $4 \times 10^9 \text{ cm}$ is then used as initial state for a simulation of the detonation flame with the LEAFS code, where the detonation is ignited at the cell with the highest temperature. For more information about the simulation see Pakmor et al. (2012a,b). The detailed composition of the material is again calculated with the tracer particle method and a post-processing step using a large nuclear reaction network (see above). The merger model yields are based on the same initial

chemical composition as the delayed-detonation model (47.5 % ^{12}C , 50.0 % ^{16}O and 2.5 % ^{22}Ne by mass). With an asymptotic kinetic explosion energy of 1.7×10^{51} erg, the merger model produced $0.616 M_{\odot}$ of ^{56}Ni out of the combined initial mass of $2.0 M_{\odot}$. In contrast to the delayed-detonation model N100, the ^{56}Ni is mainly found at velocities below $\sim 10,000 \text{ km s}^{-1}$ and it is much more asymmetrically distributed in the ejecta. This is mainly due to the delayed explosion of the secondary into the already burned remains of the primary, which excavates a region virtually free of iron group elements at low velocity (see figure 2 of Pakmor et al. 2012a).

2.2. Radiative transfer

Using detailed abundance distributions obtained from the tracer particle method we map the explosion ejecta to a $50 \times 50 \times 50$ Cartesian grid and follow the emission, propagation and interaction of the gamma-ray photons with the Monte Carlo radiative transfer code ARTIS (Sim 2007; Kromer & Sim 2009). The main principles of the radiative transport code can be summarized as follows: In contrast to Nature’s way of quantization, the radiation field is divided into Monte Carlo quanta representing indivisible parcels of energy, providing several advantages concerning the simulation technique (Lucy 1999). Initially, the quanta begin as so-called pellets of radioactive material representing ^{56}Ni , ^{56}Co , ^{52}Fe and ^{48}Cr (other radionuclides are neglected in ARTIS since they are typically not important at early times). Upon decay, the pellets are converted to mono-chromatic gamma-ray packets with frequencies sampled randomly according to the respective branching ratios. These gamma-ray packets are emitted into randomly chosen directions under the assumption of isotropic emission in the comoving frame. Then, their propagation is followed in frequency, three-dimensional space, and time, until they leave the ejecta or are removed from the gamma-ray regime due to interaction processes. The basic interaction processes of gamma-ray photons are pair production, photoelectrical absorption, and Compton scattering, with the latter being the most dominant in the encountered energy ranges (Milne et al. 2004). In accordance with the ratios of the cross sections of individual interaction processes to the total cross section, the occurrence of a certain interaction type is sampled randomly. Throughout the simulation, a positronium fraction of zero is assumed, meaning that positrons, e.g. from pair production or nuclear decays, annihilate in situ and directly lead to the production of two gamma-ray photons at 0.511 MeV (cf. Milne et al. 2004). The escaping gamma-ray packets are binned in frequency, time and direction, contributing to the spectral evolution of the gamma-ray emission from the explosion event. Light-travel time effects are taken into consideration. A thorough description of the employed Monte Carlo radiative transfer scheme and additional references can be found in Lucy (2005), Sim (2007), Sim & Mazzali (2008) and Kromer & Sim (2009).

3. Results and discussion

Even though the Chandrasekhar-mass delayed detonation and the violent merger model show distinct differences in total mass and ejecta structure, both models produce nearly the same amount of ^{56}Ni (roughly $0.6 M_{\odot}$). In spite of their differences, a straightforward preference to one of the models cannot be given by comparing the simulated optical spectra to the measured for the test case of SN 2011fe (Röpke et al. 2012). In this section, we investigate whether additional discriminating features can be

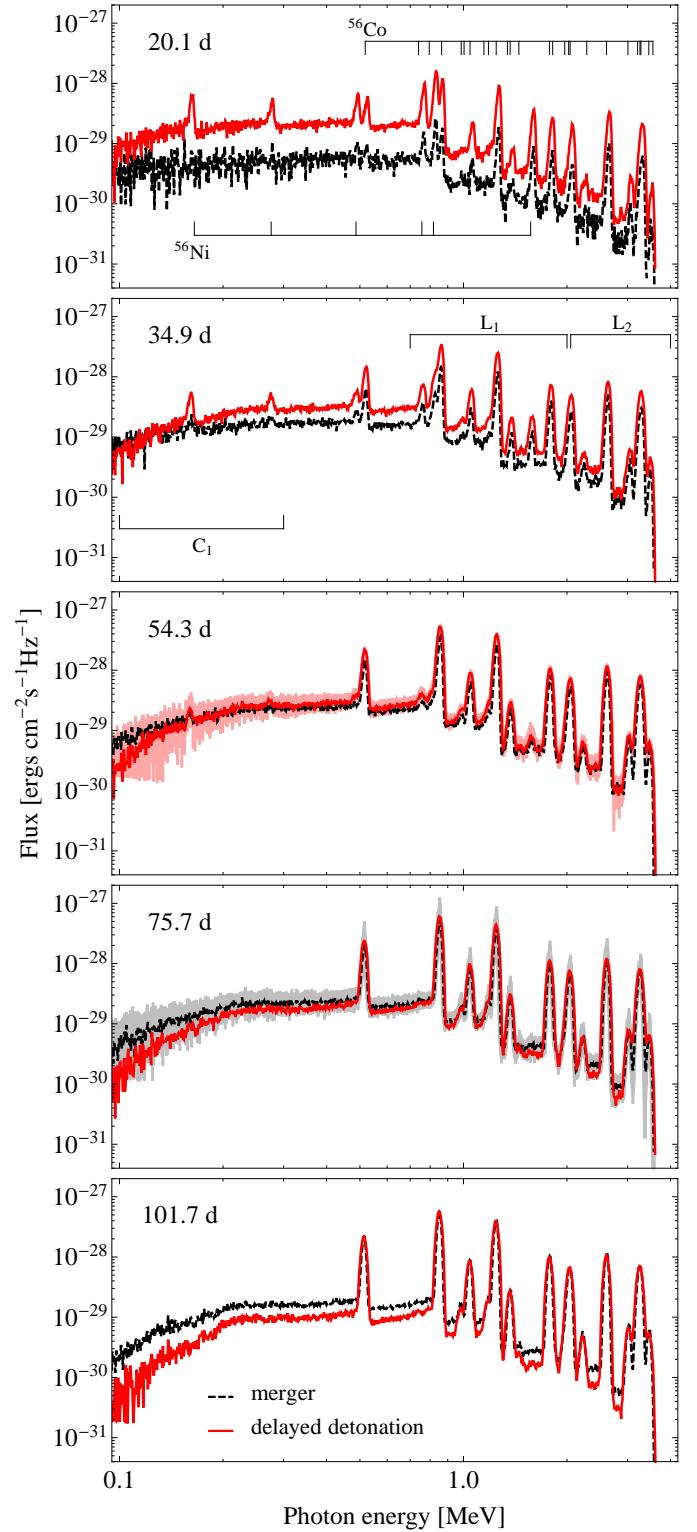


Fig. 1. Spectral evolution of the gamma-ray emission from the delayed detonation (red) and the violent merger model (dashed black) for different epochs after the explosion (indicated in the upper left of each panel). The spectral spread due to different viewing angles is shown for the maximum-light epochs of the two models in gamma rays (indicated in light red for the delayed detonation model in the third panel and in gray for the merger model in the fourth panel). Part of the effect is obscured by Monte Carlo noise in particular in the continuum. This problem is largely removed by using hardness ratios and broadband light curves. The ^{56}Ni and ^{56}Co emission lines are indicated in the first panel, the flux bands C_1 , L_1 and L_2 discussed in Sect. 3.2 are depicted in the second panel.

identified from a study of the gamma-ray emission of the two models.

3.1. Gamma-ray spectra

Fig. 1 shows the spectral evolution of the angle-averaged gamma-ray emission arising from the delayed detonation and the violent merger model (photon fluxes are always normalized to a distance of 1 Mpc). For a discussion of the importance of viewing angle effects, the reader is referred to the end of this section.

The spectra are dominated by lines of the decay chain $^{56}\text{Ni} \rightarrow ^{56}\text{Co} \rightarrow ^{56}\text{Fe}$. Due to the different half-lives of ^{56}Ni (6.1 d) and ^{56}Co (77.2 d), ^{56}Ni lines which dominate at early epochs (e.g. at 0.812 MeV or 1.562 MeV) vanish in the spectra at later times, according to the decreasing amounts of ^{56}Ni . Then, the spectra are mainly formed by strong emission lines of ^{56}Co and a continuum contribution due to Compton scattering of line photons. The optical depth to Compton scattering mainly depends on the column density of target electrons. Since the energies of gamma-ray photons of ~ 1 MeV are much higher than the corresponding binding energies of electrons in atoms, nearly all electrons, regardless if bound or unbound, are accessible as targets of Compton scattering processes. As the ejecta expand with time, optical depths are reduced, leading to an enhancement of the lines with respect to the continuum.

Besides these common properties of both explosion models, there are also some pronounced differences. The gamma-ray emission in the delayed detonation scenario evolves faster than in the WD-WD merger, a fact that is also visible in a comparison of the bolometric gamma-ray light curves (energy range from 0.05 to 4.0 MeV) of the two models (see Fig. 2, upper panel). The delayed detonation produces a peak photon flux of $1.82 \times 10^{-2} \text{ cm}^2 \text{ s}^{-1}$ at 54.3 days, whereas the merger yields a maximum flux of $1.43 \times 10^{-2} \text{ cm}^2 \text{ s}^{-1}$ at 75.7 days after the explosion. Since the masses of produced radioactive ^{56}Ni are nearly equal in both models, this is purely a consequence of the fact that the transport of gamma rays is, to first order, only sensitive to the column density of the material above the emission region. I.e. the larger total mass of the WD-WD merger delays the gamma-ray emission and gives rise to a lower (angle-averaged) peak flux compared to the delayed detonation model. The convergence of the two light curves at late times in Fig. 2 reflects the similarity of the ^{56}Ni mass in both models. In the optically thin limit, the gamma-ray luminosity is given by

$$L_\gamma(t \geq t_{\text{thin}}) \approx 1.23 \times 10^{43} \frac{M_{\text{Ni}}}{M_\odot} \exp\left(-\frac{t}{t_{\text{Co}}}\right) \text{ erg s}^{-1} \quad (1)$$

where t_{Co} is the lifetime of ^{56}Co (Sim & Mazzali 2008). Thus, if the distance to the object is known, late-time measurements of gamma-ray luminosities can be used to unambiguously determine the explosion yield of ^{56}Ni .

Another distinguishing feature can be seen in the early-time spectra of the delayed detonation model at 20.1 and 34.9 days after the explosion: While two prominent lines of ^{56}Ni can be identified at 0.158 MeV and 0.270 MeV, these two lines are nearly totally degraded in the merger model and vanish in the background of continuum emission. This effect can be explained by the energy sensitivity of the Compton cross section. Since the cross section decreases with increasing photon energy, especially lines at low energies suffer from effective Compton down-scattering and the additional contamination of likewise down-scattered higher energy photons. Therefore, the two lines can only build up if a significant amount of ^{56}Ni is located at small

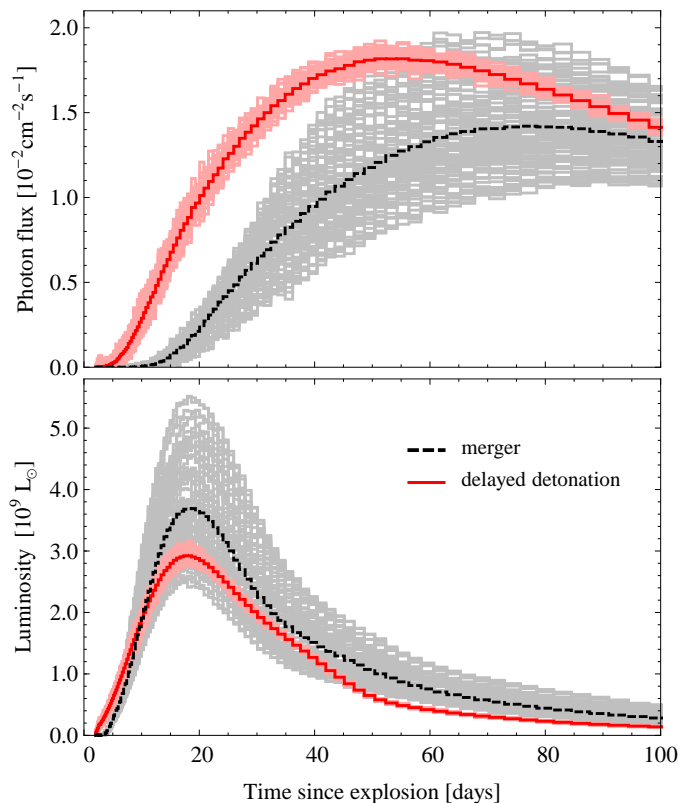


Fig. 2. Bolometric gamma-ray light curve (upper panel) and bolometric UVOIR light curve (lower panel) for the delayed detonation (red) and the violent merger model (dashed black). The light curve spread due to different viewing angles is indicated in light red and gray. The photon fluxes resp. the luminosities are normalized to a distance of 1 Mpc.

optical depths (cf. Gómez-Gomar et al. 1998), a fact that directly connects the occurrence of low-energy ^{56}Ni lines to the distribution of the radioactive material. These different distributions of ^{56}Ni can be seen in figures 1 and 2 of Röpke et al. (2012), where it is shown that there is much more ^{56}Ni at higher velocities in the delayed detonation model than in the merger model. Furthermore, there is less material surrounding the ^{56}Ni regions in the delayed detonation model and the corresponding column densities are therefore lower than in the merger scenario. This property is clearly mirrored in the evolution of the gamma-ray emission, but cannot be inferred easily from measurements in other wavelength ranges (see e.g. figure 3 in Röpke et al. 2012). The larger optical depths outside the ^{56}Ni region lead to more efficient Compton down-scattering and thus a softer spectrum of the merger model. This is further enhanced by the fact that iron-group elements are confined to lower velocities in the merger, leading to less photoelectric absorption than in the delayed detonation.

The influence of different viewing angles on the gamma-ray spectra is illustrated in Fig. 1 for the maximum-light epochs of the two models in gamma rays. While the strongest lines of the delayed detonation model do not show much variation, the asymmetric structure of the ejecta in the merger model leads to spectral features of varying magnitude, and for certain viewing angles a distinction from the spectra of the delayed detonation model can be very difficult. The low-energy range of the spectra is still the most suitable for distinguishing the two models: In the merger model, the higher column densities due to the larger total mass result in more effective Compton down-scattering of

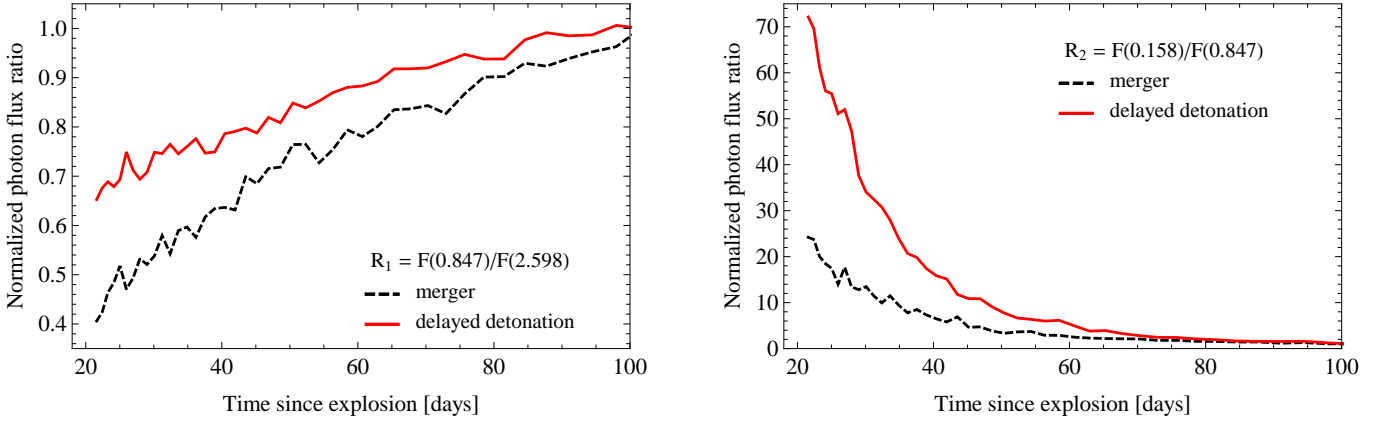


Fig. 3. Peak line flux ratios of the gamma-ray emission from the delayed detonation (red) and the violent merger model (dashed black). The graph on the left depicts the line ratio $R_1 = F(0.847 \text{ MeV})/F(2.598 \text{ MeV})$ of two ^{56}Co lines, the graph on the right illustrates the line ratio $R_2 = F(0.158 \text{ MeV})/F(0.847 \text{ MeV})$ of a ^{56}Ni and a ^{56}Co line. The flux ratios are normalized to the optically thin limit.

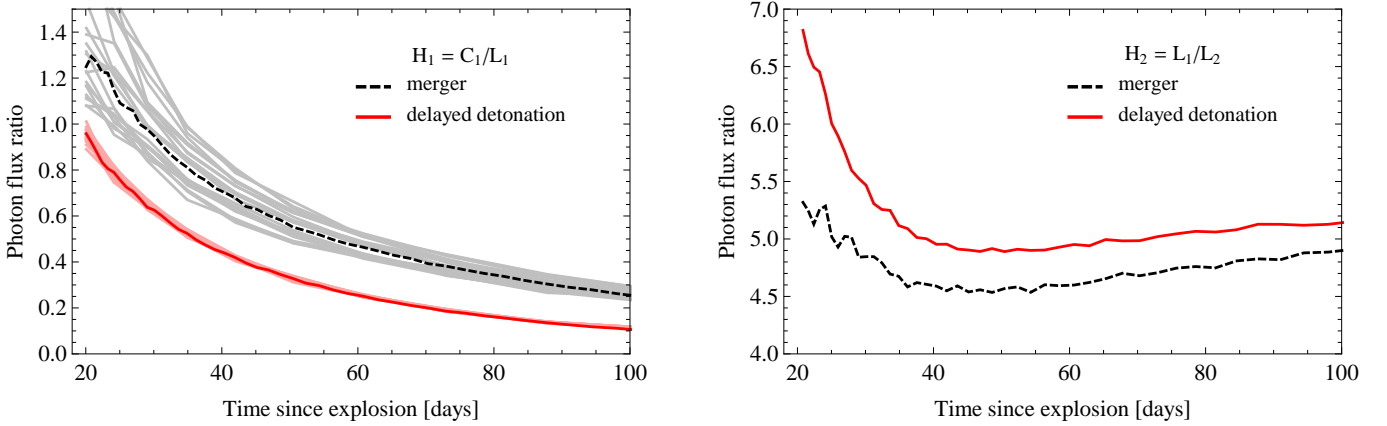


Fig. 4. Hardness ratios of the gamma-ray emission from the delayed detonation (red) and the violent merger model (dashed black). The ratio $H_1 = C_1/L_1$ is shown on the left, the ratio $H_2 = L_1/L_2$ is displayed on the right. To illustrate the sensitivity to viewing-angle effects, H_1 is shown for different lines of sight in the left panel.

the gamma-ray photons in this energy range than in the delayed detonation model. This hinders the formation of prominent low-energy ^{56}Ni lines. The effects of observing the two explosion models at different lines of sight are also illustrated for the bolometric gamma-ray light curves in Fig. 2. As before, the asymmetric distribution of ejecta in the merger model results in a much larger spread of photon fluxes compared to the delayed detonation model. Nevertheless, the different times of maximum flux, as well as the differing early time evolution of the light curves, provide clear distinctive features that can be used to discriminate the underlying explosion models. These differences are again due to the different total masses involved in the two explosion scenarios. The larger mass of the merger model leads to more efficient photon trapping at earlier times, delays the rise of the photon flux, and results in a flux peak occurring at later times.

As a comparison, we show the bolometric UVOIR light curves of the two models in the lower panel of Fig. 2. For many viewing angles, a distinction between the delayed detonation and the merger model is nearly impossible. This is contrasted by the behavior of the bolometric gamma-ray light curves: Here, in spite of viewing angle effects, especially early time measurements as well as the determination of the maximum fluxes are very promising. This again underlines the advantages of gamma-ray emission studies of SNe Ia.

In the following, we discuss further possibilities to discriminate the two explosion models on the basis of angle-averaged spectra and present the fundamental distinguishing characteristics. As described in the previous paragraph, viewing-angle effects can considerably complicate the process of drawing inferences about certain explosion scenarios, but distinctions are still possible.

3.2. Line and hardness ratios

In addition to the analysis of line fluxes and light curves, line and hardness ratios represent further diagnostic tools that can be utilized for the study of the gamma-ray emission of SNe Ia (cf. Höflich et al. 1998; Gómez-Gomar et al. 1998; Sim & Mazzali 2008). While the information inferred from absolute flux values is always restricted by how well the distance to the source is known, flux ratios are distance-independent and not subject to this limitation. In Fig. 3, two characteristic peak-intensity line ratios of the WD-WD merger and the delayed detonation model are illustrated. Following Sim & Mazzali (2008) we define $R_1 = F(0.847 \text{ MeV})/F(2.598 \text{ MeV})$ as the ratio of two ^{56}Co lines and $R_2 = F(0.158 \text{ MeV})/F(0.847 \text{ MeV})$ as the ratio of a ^{56}Ni and a ^{56}Co line.

Flux ratios are affected by similar processes as discussed in the previous paragraph: Due to the energy sensitivity of Compton cross sections, line ratios are, at early times before the optically thin limit, dependent on the column density of electrons and therefore on the material above the region containing the radioactive species. The ratio of two lines of the same radioactive isotope is therefore determined by the opacity ratios at the respective line energies. This is shown in the left plot of Fig. 3 for the case of R_1 . Since the radioactive material in the merger model is behind much more opacity, the line ratio shortly after the explosion is much lower. This is different in the delayed detonation model: Here, more ^{56}Ni and hence more ^{56}Co at lower optical depths increases the line ratio significantly. It is thereby not crucial to choose two specific ^{56}Co lines for the examination of such an effect, but the extent of the diagnostic validity relies, due to the energy dependence of the Compton cross section, on a sufficient spread between the energy of the two selected lines (cf. Sim & Mazzali 2008).

In contrast to R_1 , R_2 is a function that decreases with time. Since R_2 is a ratio of two lines from different isotopes, this behavior reflects the difference between the half-lives of ^{56}Ni and ^{56}Co : While the ^{56}Co line at 0.847 MeV strengthens, the 0.158 MeV line of ^{56}Ni fades away at later times, leading to smaller peak flux ratios. The information value of R_2 is based on the following aspect: As discussed before, the ^{56}Ni present in the outer shells at small optical depths is the main source of the emerging 0.158 MeV line, whereas the emission of the 0.847 MeV line originates from the total abundance of ^{56}Co in the ejected material, especially at later times. Therefore, a larger value of R_2 indicates a larger deposit of ^{56}Ni in the outer layers of the ejecta and the different distributions of this isotope in the two models are clearly reflected in the evolution of the line ratios shown in Fig. 3. As stated before (Gómez-Gomar et al. 1998; Sim & Mazzali 2008), the relatively low energy of the 0.158 MeV line makes it also very sensitive to photoelectric absorption processes. Since photoelectric opacities are dependent on the compositional structure of the ejecta above the radioactive material, appropriate ratios of low-energy ^{56}Ni lines to ^{56}Co lines at higher energies are well suited to study the composition of SNe Ia. The success in finding distinct abundance features of course relies on the quality of the measured gamma-ray data and for this reason also on the distance to the explosion site (see also the remarks in the next section).

A way to partially circumvent the need for highest quality gamma-ray data for detailed SNe Ia studies is provided by the application of hardness ratios. Instead of discrete line intensities, the fluxes of broader energy bands are compared to each other. On the one hand, in this coarser method, some information is necessarily lost. But on the other hand, in contrast to other wavelength ranges, the relative simplicity of gamma-ray spectra and the rather small number of factors that influence gamma-ray emission processes make hardness ratios an important diagnostic tool. Following Sim & Mazzali (2008), Fig. 4 shows two hardness ratios, $H_1 = C_1/L_1$ and $H_2 = L_1/L_2$, as examples for the delayed detonation and the merger model. C_1 denotes the energy band from 0.1 to 0.3 MeV, where the main contribution comes from continuum emission by Compton down-scattering and photo-absorption processes. The energy bands L_1 (from 0.7 to 2.0 MeV) and L_2 (from 2.0 to 4.0 MeV) are characterized by pronounced lines of ^{56}Co , while the importance of continuum emission decreases with higher photon energies.

Similar to line ratios, hardness ratios are mainly affected by the energy dependence of the Compton cross section. Since H_1 directly mirrors the strength of the continuum emission relative

to that of the lines, the violent merger produces higher H_1 values than the delayed detonation – a direct consequence of the radioactive material’s location at higher optical depths. Similar to the line ratio R_2 , H_1 is an indicator of different column densities of target electrons. Since photoabsorption processes can be significant in the energy band C_1 , H_1 also serves to a certain degree as an indicator of different compositions. H_2 represents the flux ratio of two line-dominated energy bands and is analogous to the line ratio R_1 . It depends mainly on the ratio of the Compton cross sections in the two corresponding energy bands and is also suitable to discriminate our explosion models. Hence, hardness ratios offer an alternative opportunity to extract information from the gamma-ray emission of SNe Ia – particularly for more distant explosion events.

The results in Fig. 3 and 4 show that line and hardness ratios can be used as additional diagnostic tools to distinguish the delayed detonation from the merger model on the basis of their gamma-ray emission. These ratios are directly linked to the distribution of ^{56}Ni in the ejecta and, due to their dependence on the column density of target electrons above the radioactive material, they are sensitive to different compositions and masses of the outer ejecta layers. Even in light of possible viewing angle effects (see left panel of Fig. 4 as an example), hardness ratios have proven to be quite robust in distinguishing our two models. Together with broadband light curve measurements, they provide the best chances for conclusions on certain model features especially for more distant explosion events.

However, besides the changes in the gamma-ray emission due to different viewing angles, other variations within a certain explosion scenario (e.g. additional rotation and mixing effects, modifications of details in the explosion mechanism) can lead to a spread in gamma-ray fluxes that makes it certainly very difficult to distinguish between different realizations of SN Ia explosions. But concerning our two very different models representing two different progenitor classes, we are confident that the delayed detonation and the violent merger as described above will leave a unique imprint on the gamma-ray emission: In the case of the same ^{56}Ni mass in both models, a higher total ejecta mass surrounding the radioactive material in the applied violent merger is unavoidable. Corresponding to our results that we have discussed before, this has a systematic effect on the gamma-ray observables. As we will show in the next section, the prospects for discriminating our two models in case of a nearby SN Ia are very promising, but rely on the realization of new MeV satellite missions in the near future.

4. Detection prospects

Despite the importance of the MeV energy range for the study of different astrophysical objects and processes (cf. Greiner et al. 2012; Summa et al. 2011), the mission with the highest sensitivities at these energies was the COMPTEL instrument aboard the CGRO satellite in the mid-nineties. One possible successor with an enhanced sensitivity of a factor 40 is the proposed GRIPS (Gamma-Ray Imaging, Polarimetry and Spectroscopy) mission (Greiner et al. 2009, 2012). The focus of this section is on the progress that could be made in the future concerning the detection of gamma-ray emission from SNe Ia, using the GRIPS instrument as an example.

Being able to detect photons with energies from 0.2 MeV to 80 MeV, GRIPS is specifically designed for the search of gamma-ray bursts and blazars, the study of particle acceleration and radiation processes in a variety of cosmic sources, and the study of supernova explosion and nucleosynthesis mechanisms.

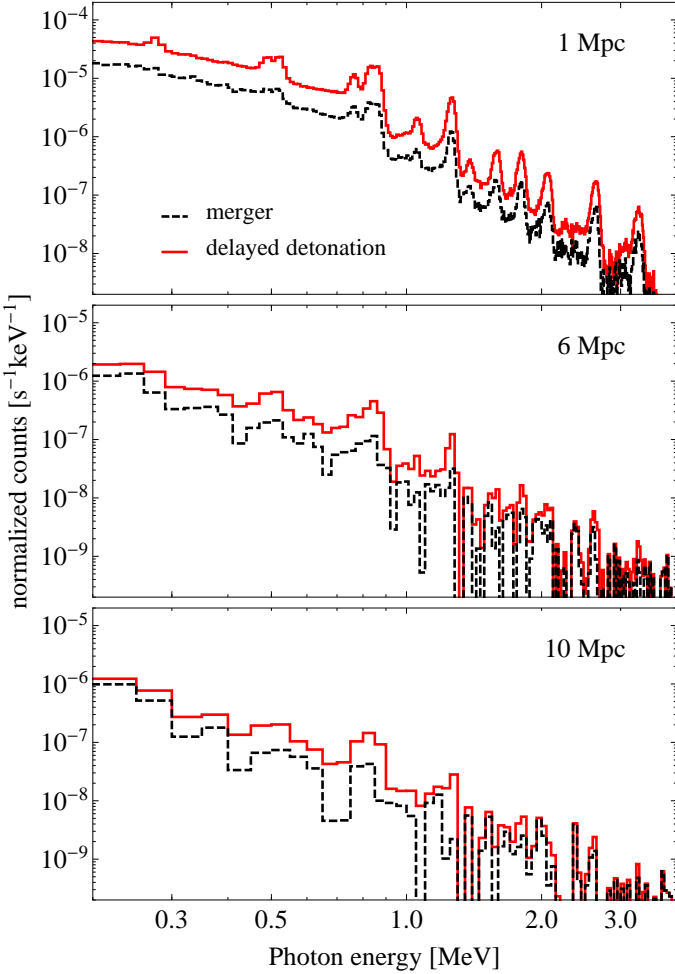


Fig. 5. Simulated detector response for the GRM instrument aboard GRIPS using an exposure time of 10^5 s. Shown is a comparison of the simulated angle-averaged gamma-ray spectra of the delayed detonation model (red) and the merger model (dashed black) at 25 days after the explosion for different distances to the source (indicated in the upper right).

The main instrument of GRIPS is the Gamma-Ray Monitor (GRM), a combined Compton scattering and pair creation telescope consisting of two separate detectors with an effective area of 195 cm^2 and an energy resolution of 17 keV at 1.8 MeV . The so-called *tracker*, made of silicon strips, is the first detector where the initial interaction of the incoming gamma-ray photons takes place. Except for the entrance surface it is surrounded by the second detector, a calorimeter composed of LaBr_3 scintillator material that allows for the energy determination of the secondary particles. In the case of a Compton scattering event in the tracker, the incident gamma-ray photon interacts with an electron, whose energy and position can be measured. The scattered photon is recorded in the calorimeter where its energy and interaction point can be reconstructed. With these data, it is possible to calculate the direction and the energy of the incident photon. In the case of a pair creation event, the incident gamma-ray photon is converted into an electron-positron pair within the first detector. The original direction of the incident photon can be determined from the tracked directions of these two particles. The energy of the two secondaries, and therefore the energy of the incident photon, is measured with the help of both the tracker and the calorimeter.

GRIPS measurements of gamma-ray emission from SNe Ia were simulated using the MEGALIB software package (Zoglauer et al. 2006). This package uses the GEANT4 toolkit (Agostinelli et al. 2003) to simulate the passage of gamma rays and other particles through the detector, taking into account possible particle interactions and decays. The detector response to an incident gamma photon is calculated from the energies deposited by the particles in sensitive elements (silicon strips and scintillator crystals), taking into consideration instrumental effects such as the energy resolution and noise suppression thresholds. MEGALIB includes a dedicated event reconstruction algorithm, which is applied to the events that pass the trigger criteria (coincident hits in the silicon strip detector and the calorimeter). This algorithm either reconstructs the event as a valid Compton scattering or pair creation event, or rejects it. In the case of a Compton event, the incident photon direction is constrained to a circle around the direction of the scattered photon. To select the events compatible with the source position of the photons, we required the minimum distance between the circle and the source position to be less than 2° . In addition, if the recoil electron left a track in the silicon detector, the Compton scattering plane could be reconstructed and its rotation angle around the direction of the scattered photon was required to be within 30° from the source position. The model of the GRM detector used in this study corresponds to the setup described in Greiner et al. (2012).

Measurements of gamma-ray emission from most sources are strongly affected by the presence of radiation backgrounds. In our simulations we include the background from diffuse cosmic photons based on Gruber et al. (1999) and the background from albedo photons produced in the Earth’s atmosphere (Mizuno et al. 2004; Ajello et al. 2008). In Boggs (2006) these two components were found to be the dominating background for a Compton telescope at a low-inclination low Earth orbit. The generated background photons were processed through the same simulation and selection procedure described above and then the reconstructed background events were added to the source events.

In order to account for the specific sensitivity range of GRIPS, we define here the hardness ratio H_1^* analogous to H_1 as the quotient C_1^*/L_1 , where C_1^* denotes the energy band from 0.2 to 0.4 MeV . In Fig. 5, the simulation results for the measured gamma-ray spectra are shown for the two models at 25 days after the explosion. The exposure time of 10^5 s corresponds to roughly 5 days in the all-sky scanning mode of GRM, a time interval that allows for reasonable studies of the time evolution. Accurate measurements of the line and hardness ratios become difficult for large source distances due to background fluctuations and limited event statistics in the high energy part of the spectrum. For the GRIPS mission, nearly the best discrimination between the two explosion models is provided by measurements of the H_1^* hardness ratio. The simulation outcomes of the measurement of H_1^* are depicted in Fig. 6. This ratio can be used to distinguish the models up to a source distance of 5 to 7 Mpc . Our simulation results for light curve measurements are shown in Fig. 7. For a supernova event at a distance of 1 Mpc , a very detailed and accurate light curve can be measured and constraints on certain explosion models are possible. According to our analysis of light curve measurements, GRIPS should be able to easily distinguish the two explosion scenarios for a source distance up to 10 Mpc .

Using the gamma-ray spectrum of the delayed detonation model at 60 days after the explosion as input, we additionally carried out detector response simulations for different source distances and a longer exposure time of 10^6 s (roughly 12 days

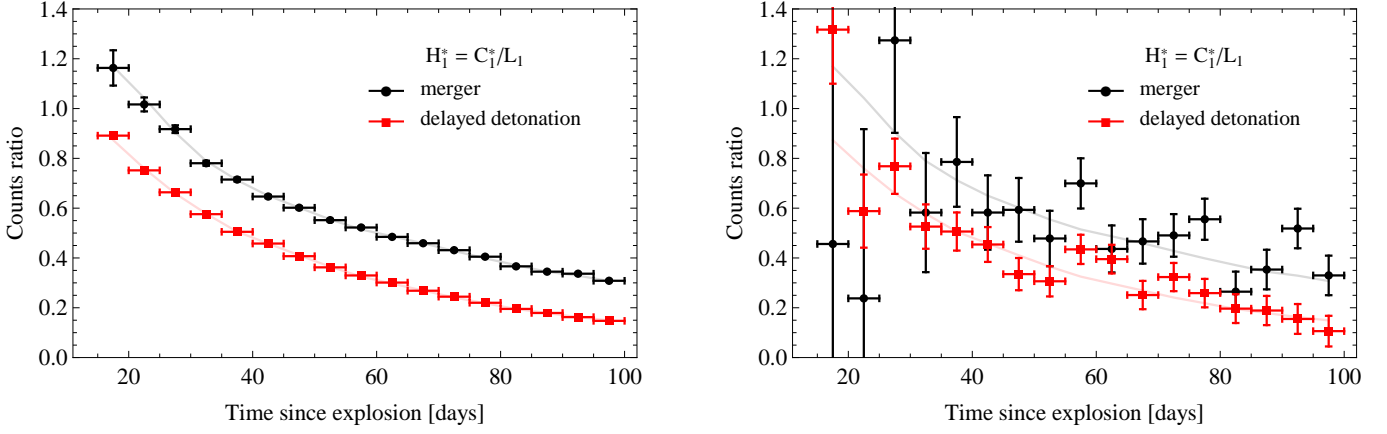


Fig. 6. Simulation results for hardness ratio measurements with the GRM instrument (exposure time 10^5 s) for our two explosion models. On the left, a source distance of 1 Mpc is assumed, the right figure shows the results for a source distance of 5 Mpc. Taking into account the sensitivity limits of GRIPS, C_1^* here denotes the energy band from 0.2 to 0.4 MeV. The solid lines show the results of ideal measurements without background fluctuations and statistical errors.

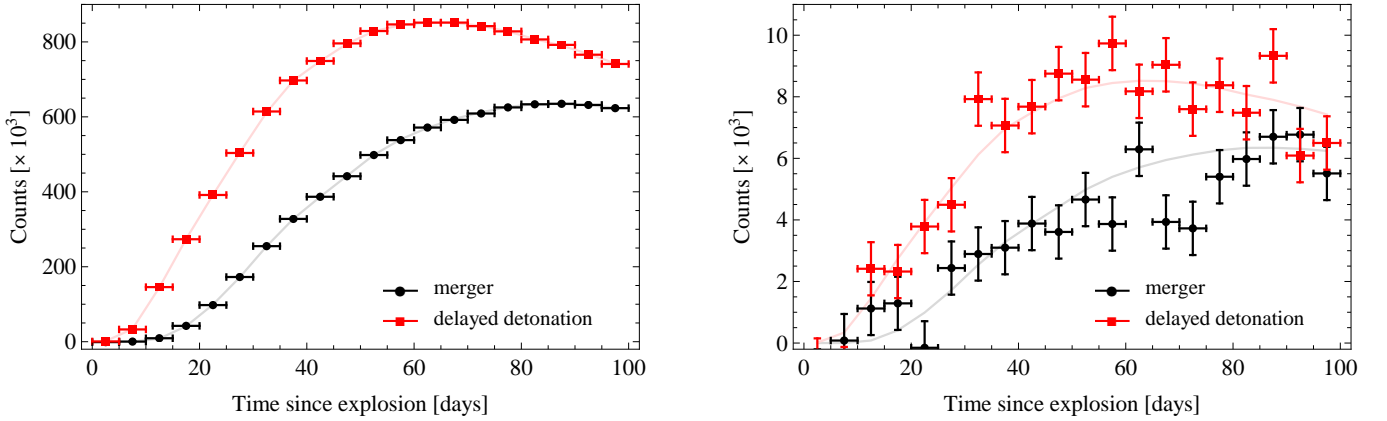


Fig. 7. Simulation results for light curve measurements (energy range from 0.4 to 4.0 MeV) with the GRM instrument (exposure time 10^5 s) for our two explosion models. On the left, a source distance of 1 Mpc is assumed, the right figure shows the results for a source distance of 10 Mpc. The solid lines show the results of ideal measurements without background fluctuations and statistical errors.

in on-axis pointing mode). The detection capabilities of GRIPS concerning the gamma-ray emission of SNe Ia are illustrated in Fig. 8, where the simulated measurements after background subtraction are depicted. While the strongest lines at medium and higher energies can still be resolved even for sources at 20 Mpc and more, the low energy range of the measured spectra from sources at larger distances is dominated by background fluctuations. Although GRIPS will provide a spectral resolution of all details in the energy range from 0.2 to 80 MeV only for SNe Ia at distances up to a few Mpc, the application of line and hardness ratios enables valuable spectral studies for even larger distances. For an exposure time of 10^6 s, our simulations show that the hardness ratio H_1^* can be used to distinguish the two models up to 10 Mpc. With this longer exposure time, GRIPS light curve measurements can serve as distinctive marks of our models up to distances of 15 to 16 Mpc. Even explosion events in the Virgo cluster will be accessible for gamma-ray studies with such an instrument.

The success of such investigations of course depends on the accuracy of the applied background models (see above). According to Ajello et al. (2008), an uncertainty of a factor of three seems to be quite reasonable. Although the chances for a clear discrimination between certain explosion models decrease

considerably for larger source distances, the ability of GRIPS in proving the gamma-ray emission of SNe Ia at distances beyond 20 Mpc will lead to a significant improvement of SNe Ia detection statistics in the gamma-ray energy range. Due to the low sensitivities of previous gamma-ray observatories, only one SN Ia has been detected up to now (cf. Milne et al. 2004).

In cases of events comparable to SN 2011fe, the detection of gamma-ray emission should be easily possible with an instrument like GRIPS. Our simulation results show that important constraints on three-dimensional explosion models can be drawn immediately. Since the limited sensitivity of GRIPS below 300 keV hinders a thorough examination of this energy range for sources at larger distances, the ^{56}Ni lines at 0.158 MeV and 0.270 MeV, which can serve as important diagnostic tools (see also section 3.1), are not so easily accessible. This problem can be cured by combining the gamma-ray data of GRIPS with the data of the likewise proposed ASTRO-H mission (cf. Takahashi et al. 2010) that covers the respective energy range with sufficient sensitivity. A recent study concerning the detection capabilities of ASTRO-H shows that distance limits comparable to those of the GRIPS mission can be reached (Maeda et al. 2012). The realization of two missions with sensitivities and photon energy coverages like GRIPS and ASTRO-H in

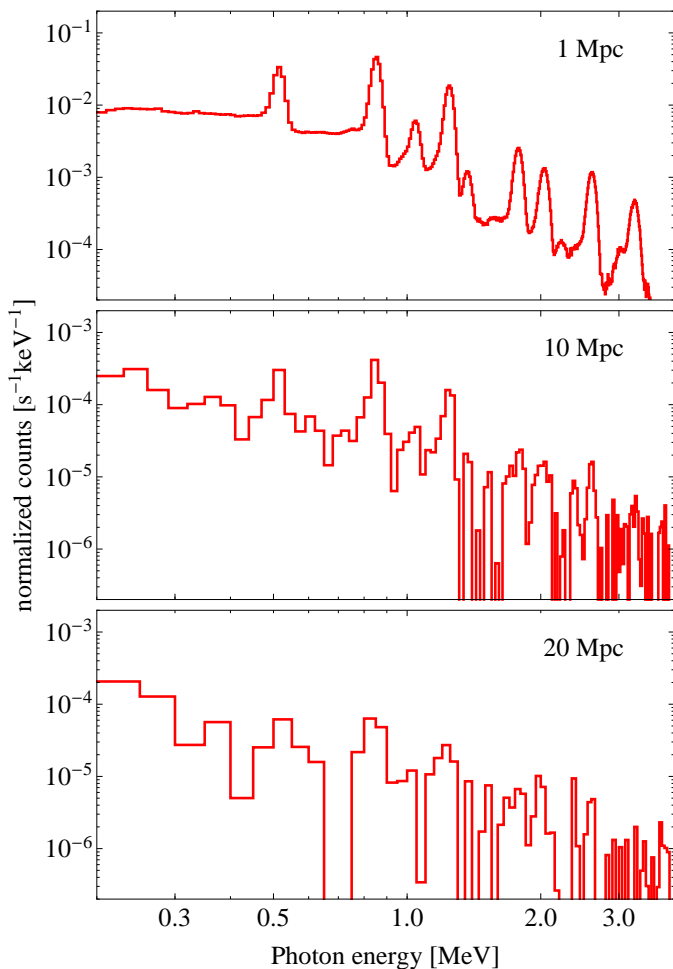


Fig. 8. Simulated detector response for the GRM instrument aboard GRIPS for an exposure time of 10^6 s. Shown is the simulated angle-averaged gamma-ray spectrum of the delayed detonation model at 60 days after the explosion for different source distances (indicated in the upper right).

the near future would therefore offer unprecedented detection prospects for the gamma-ray emission of SNe Ia and equally support the efforts in reducing the parameter space of current three-dimensional model concepts. Especially the degeneracy concerning optical observables of different explosion models for the recent explosion event SN 2011fe (cf. Röpke et al. 2012) could be certainly removed by a study of the corresponding gamma-ray emission as shown in the previous paragraphs.

5. Conclusions

Using three-dimensional simulations of a delayed detonation of a Chandrasekhar-mass WD and a violent merger of two WDs as test cases, we show that the calculated gamma-ray spectra are well-suited to draw conclusions on the different ejecta structure of the two models, but viewing angle effects always have to be taken into account. The direct link of gamma-ray spectra to the abundance of ^{56}Ni – the radioactive isotope that powers the radiation in all other wavelength bands – and their reduced complexity due to their straightforward connection to fundamental physical processes make them a promising utility that can be used in a complementary way to other measurements. Being mainly sensitive to the column density of the material above the emis-

sion region, the gamma-ray emission of SNe Ia is well suited to study the composition as well as the total mass of the ejecta. Our analysis of different diagnostic tools such as line and hardness ratios demonstrates that especially hardness ratios offer the best prospects to distinguish the two models at further distances. We also underline the value of following the evolution of gamma-ray emission over an extended period of time: Even low-resolution spectra of distant explosion events lead to characteristic light curve shapes that allow a discrimination of the two models. If the flux maximum can be obtained to a precision of about 5 days, bolometric measurements are sufficient to discriminate the two models. The prospects of success of course depend on the future development in the sector of detection instruments. Concerning the sensitivities in the hard X-ray as well as in the soft gamma-ray range, a major step forward will be done with the planned ASTRO-H satellite and the proposed GRIPS mission, allowing for observations of gamma-ray emission from SNe Ia up to 20 Mpc according to conservative estimates. Although a spectral resolution of all line features will only be provided for nearby explosion events, our simulated GRIPS observations show that hardness ratio and light curve measurements can discriminate our models up to source distances of 10 to 16 Mpc, dependent on the applied exposure time. This enhances the number of target candidates in the MeV energy range significantly and will allow for more meaningful gamma-ray emission studies of SNe Ia than up to now, including potentially unique opportunities for model discrimination.

Acknowledgements. This work was in parts funded by the Deutsche Forschungsgemeinschaft (DFG) through the graduate school on “Theoretical Astrophysics and Particle Physics” (GRK 1147). The work of F. K. Röpke and M. Fink was supported by the Deutsche Forschungsgemeinschaft via the Emmy Noether Program (RO 3676/1-1) and by the ARCHES prize of the German Federal Ministry of Education and Research (BMBF). Funding for collaboration was provided by the DAAD/Go8 German-Australian exchange program. The work of A. Ulyanov was supported under ESA’s Strategic Initiative AO/1-6418/10/NL/Cbi. K. Maeda received support from the World Premier International Research Center Initiative (WPI Initiative), MEXT, Japan. The simulations presented in this work were carried out at the Jülich Supercomputing Centre (Germany) as part of the projects HMU14 and PRA026 within the Partnership for Advanced Computing in Europe (PRACE). The GRIPS/GRM model used in this work was developed by A. Zoglauer. The GRIPS simulations were performed using the UCD Pascal cluster funded through the SFI Equipment Grant for High-Performance Computing Cluster. This work was supported by the NCI National Facility at the Australian National University.

References

- Agostinelli, S., Allison, J., Amako, K., et al. 2003, Nuclear Instruments and Methods in Physics Research A, 506, 250
- Ajello, M., Greiner, J., Sato, G., et al. 2008, ApJ, 689, 666
- Ambwani, K. & Sutherland, P. 1988, ApJ, 325, 820
- Blondin, S., Mandel, K. S., & Kirshner, R. P. 2011, A&A, 526, A81+
- Boggs, S. E. 2006, New A Rev., 50, 604
- Burrows, A. & The, L.-S. 1990, ApJ, 360, 626
- Chan, K.-W. & Lingenfelter, E. R. 1990, in International Cosmic Ray Conference, Vol. 1, International Cosmic Ray Conference, 101
- Chan, K. W. & Lingenfelter, R. E. 1988, in American Institute of Physics Conference Series, Vol. 170, Nuclear Spectroscopy of Astrophysical Sources, ed. N. Gehrels & G. H. Share, 110–115
- Chan, K. W. & Lingenfelter, R. E. 1991, ApJ, 368, 515
- Clayton, D. D. 1974, ApJ, 188, 155
- Clayton, D. D., Colgate, S. A., & Fishman, G. J. 1969, ApJ, 155, 75
- Dan, M., Rosswog, S., Guillochon, J., & Ramirez-Ruiz, E. 2011, ApJ, 737, 89
- Gómez-Gomar, J., Isern, J., & Jean, P. 1998, MNRAS, 295, 1
- Greiner, J., Iyudin, A., Kanbach, G., et al. 2009, Experimental Astronomy, 23, 91
- Greiner, J., Mannheim, K., Aharonian, F., et al. 2012, Experimental Astronomy, 34, 551
- Gruber, D. E., Matteson, J. L., Peterson, L. E., & Jung, G. V. 1999, ApJ, 520, 124

- Hillebrandt, W. & Niemeyer, J. C. 2000, *ARA&A*, 38, 191
Höflich, P. 2002, *New A Rev.*, 46, 475
Höflich, P., Khokhlov, A., & Müller, E. 1992, *A&A*, 259, 549
Höflich, P., Wheeler, J. C., & Khokhlov, A. 1998, *ApJ*, 492, 228
Isern, J., Bravo, E., & Hirschmann, A. 2008, *New A Rev.*, 52, 377
Kasen, D., Röpke, F. K., & Woosley, S. E. 2009, *Nature*, 460, 869
Khokhlov, A. M. 1991, *A&A*, 245, 114
Kromer, M. & Sim, S. A. 2009, *MNRAS*, 398, 1809
Kromer, M., Sim, S. A., Fink, M., et al. 2010, *ApJ*, 719, 1067
Kumagai, S. & Nomoto, K. 1997, in *NATO ASIC Proc. 486: Thermonuclear Supernovae*, ed. P. Ruiz-Lapuente, R. Canal, & J. Isern, 515
Lucy, L. B. 1999, *A&A*, 344, 282
Lucy, L. B. 2005, *A&A*, 429, 19
Maeda, K., Terada, Y., Kasen, D., et al. 2012, submitted
Mazzali, P. A., Röpke, F. K., Benetti, S., & Hillebrandt, W. 2007, *Science*, 315, 825
Milne, P. A., Hungerford, A. L., Fryer, C. L., et al. 2004, *ApJ*, 613, 1101
Mizuno, T., Kamae, T., Godfrey, G., et al. 2004, *ApJ*, 614, 1113
Müller, E., Höflich, P., & Khokhlov, A. 1991, *A&A*, 249, L1
Pakmor, R., Edelson, P., Röpke, F. K., & Hillebrandt, W. 2012a, *MNRAS*, 424, 2222
Pakmor, R., Hachinger, S., Röpke, F. K., & Hillebrandt, W. 2011, *A&A*, 528, A117
Pakmor, R., Kromer, M., Röpke, F. K., et al. 2010, *Nature*, 463, 61
Pakmor, R., Kromer, M., Taubenberger, S., et al. 2012b, *ApJ*, 747, L10
Reinecke, M., Hillebrandt, W., Niemeyer, J. C., Klein, R., & Gröbl, A. 1999, *A&A*, 347, 724
Röpke, F. K., Gieseler, M., Reinecke, M., Travaglio, C., & Hillebrandt, W. 2006, *A&A*, 453, 203
Röpke, F. K. & Hillebrandt, W. 2005, *A&A*, 431, 635
Röpke, F. K., Kromer, M., Seitenzahl, I. R., et al. 2012, *ApJ*, 750, L19
Röpke, F. K. & Niemeyer, J. C. 2007, *A&A*, 464, 683
Schmidt, W., Niemeyer, J. C., Hillebrandt, W., & Röpke, F. K. 2006, *A&A*, 450, 283
Seitenzahl, I. R., Ciaraldi-Schoolmann, F., Röpke, F. K., et al. 2013, *MNRAS*, 429, 1156
Seitenzahl, I. R., Meakin, C. A., Townsley, D. M., Lamb, D. Q., & Truran, J. W. 2009, *ApJ*, 696, 515
Seitenzahl, I. R., Röpke, F. K., Fink, M., & Pakmor, R. 2010, *MNRAS*, 407, 2297
Sim, S. A. 2007, *MNRAS*, 375, 154
Sim, S. A. & Mazzali, P. A. 2008, *MNRAS*, 385, 1681
Springel, V. 2005, *MNRAS*, 364, 1105
Summa, A., Elsässer, D., & Mannheim, K. 2011, *A&A*, 533, A13
Takahashi, T., Mitsuda, K., Kelley, R., et al. 2010, in *Society of Photo-Optical Instrumentation Engineers (SPIE) Conference Series*, Vol. 7732, Society of Photo-Optical Instrumentation Engineers (SPIE) Conference Series
Travaglio, C., Hillebrandt, W., Reinecke, M., & Thielemann, F.-K. 2004, *A&A*, 425, 1029
Zoglauer, A., Andrichke, R., & Schopper, F. 2006, *New A Rev.*, 50, 629